Dynamic Simulation of a Photovoltaic Refrigeration System

Athula Rajapakse
Energy Technology Program, Asian Institute of Technology
GPO Box 2754, Bangkok 10501, Thailand

Supachart Chungpibulpatana
National Science and Technology Development Agency
Gypsum Metropolitan Tower, 18th Floor, 593/2 Sri-Ayudhya Rd.
Rajdhevee, Bangkok 10400, Thailand

ABSTRACT

Dynamic behavior of a photovoltaic (PV) refrigeration system is complex due to the statistical nature of solar radiation and the interaction among system components. Analysis of the output and the reliability of such a system requires computer simulation. This paper presents mathematical models for the main system components, namely the photovoltaic array, the battery, the charge regulator and the refrigerator. Various parameters in the above models are evaluated either by using the manufacturer's data for the relevant component or through experimental tests. These four component models are then appropriately linked to develop the PV refrigeration system simulation program. The validity of the mathematical models was experimentally investigated and the results are presented. Results show that the developed model can predict the performance fairly well. Also, the drawbacks in the model, which can be rectified in a later study, are identified and discussed in the paper.

1. INTRODUCTION

In recent years, the use of solar photovoltaic (PV) refrigerators in vaccine cold chains has been promoted by the Expanded Program on Immunization (EPI) of the World Health Organization (WHO). Zaffran [1] reports that there are around 3500 solar PV refrigeration systems installed throughout the world. Most of these are located in the remote areas of the developing countries and have substantially improved the reliability and sustainability of vaccine cold chains in those remote areas. Although the technology of solar PV refrigeration is now mature, there are still technical failures which result from the problems relating to the system component selection, and system design and optimization.

The sizing of the components of a PV refrigeration system requires the analysis of its feasibility in terms of desired output and reliability with respect to the climatological data of the location where the refrigerator is to be installed. Such an analysis requires detailed computer simulations, which take into account the statistical nature of solar radiation and the dynamic effects of interaction between different system components.

Detailed computer simulation requires a significant amount of effort, expertise and expense, and hence it may be excessive for system design purposes, especially for small systems. Therefore, most of the manufacturers use simplified methods based on monthly average daily totals of the solar radiation and the average daily load, for system component sizing, which may not always

lead to the correct design. However, an experimentally validated, detailed simulation program can be conveniently used for investigating the accuracy of simplified sizing methods and to check the appropriateness of designs already made with simplified methods.

The main objective of the study presented in this paper is to develop a simulation model to predict the performance of a photovoltaic refrigeration system (including power consumption and temperatures of the vaccine load and ice-packs stored in the refrigerator) under variable climatic conditions. The above objective is achieved through improvement of the existing models and test procedures for PV array, battery and controller, development of a model for a vaccine refrigerator with two separate compartments for cold storage and ice-pack freezing and employing two separate compressors, and experimental validation of the simulation model under actual operating conditions.

This study focuses only on the refrigerators for vaccine storage which require storing temperature between 0°C and 8°C and a minimum ice making capacity of 2.0 kg per day. The effect of door opening for unloading vaccine and ice-packs on the performance of the refrigerator is not considered. The scope of the study is restricted to only one type of PV refrigerator due to the limited time available for the study.

The paper is organized in the following manner. After the brief description of the PV refrigeration system, models of four main components in the PV refrigeration system are presented. Then the details of the experimental validation are given and the results of the study are discussed. The concluding remarks are given in the final section. The detailed procedures for determination of model parameters are given in the Appendices.

2. PHOTOVOLTAIC REFRIGERATION SYSTEM

A stand-alone PV refrigeration system shown in Fig.1 basically consists of a photovoltaic array, a controller, a storage battery and a refrigerator. The PV array, which generally consists of several PV modules, produces DC electricity when it is exposed to sunlight. This electricity is then transmitted to the controller via electrical cables. The controller, which is an electronic device, protects the battery by preventing it from being excessively charged or discharged. The storage battery is used to store the excess energy produced during sunshine periods. This stored energy is used to run the refrigerator when solar radiation is not available. The refrigerator produces the cooling effect by running a vapor compression refrigeration cycle, which mostly uses a hermetically sealed 12V DC compressor.

3. THEORETICAL MODEL OF THE PHOTOVOLTAIC ARRAY

For a system operating in "clamped voltage mode" as in PV refrigeration systems, the output voltage, V, of the PV array is fixed at the system's operating voltage which is approximately equal to the battery voltage. The output current, I_p, of a PV panel connected to such a system can be expressed as

$$I_p = I_L - I_O \left[\exp\left(\frac{q(V + I_p R_s)}{A k T_p} \right) - 1 \right] - \left(\frac{V + I_p R_s}{R_{sh}} \right) \quad (1)$$

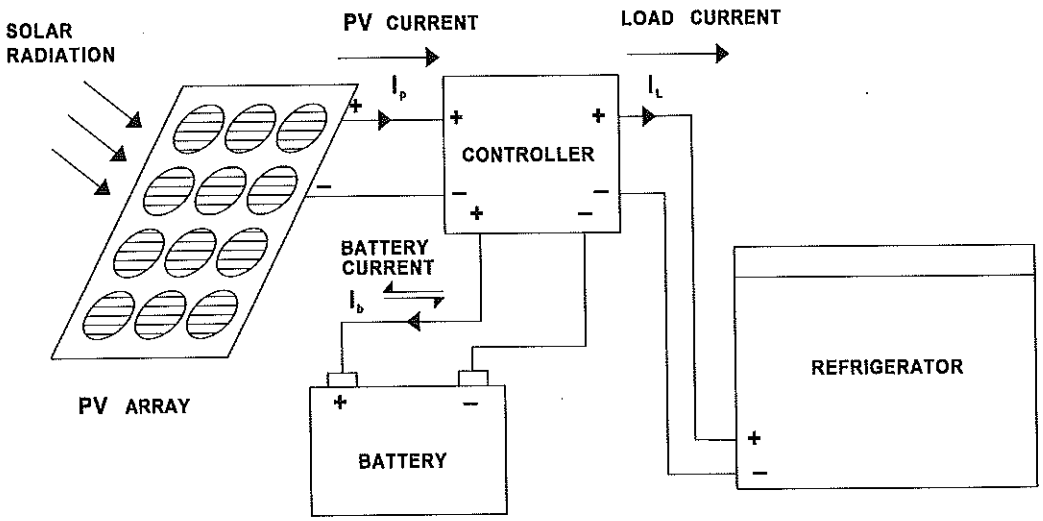

Fig. 1. A stand-alone photovoltaic refrigeration system.

where V = Terminal voltage for module (V), I_p = Output current of panel (A), I_L = Light generated current per module (A), I_o = Reverse saturation current per module (A), R_s = Series resistance per module (ohms), R_{sh} = Shunt resistance per module (ohms), q = Electron charge (1.6×10^{-19} C), A = Diode ideality factor for module, k = Boltzmann constant (1.38×10^{-23} J/K) and T_p = Cell temperature (K).

The values of R_s, R_{sh} and A in Eq.(1) are constants for a particular PV module. I_L depends upon the incident radiation on the module and the cell operating temperature. I_o is basically a function of cell temperature only. Cell temperature T_p is affected by factors such as global radiation, ambient temperature, wind speed and the electrical load on panel.

Under short circuit conditions, the panel current and the light generated current in Eq.(1) become equal to the short circuit current, I_{sc} (i.e., $I_p = I_L = I_{sc}$) since R_s is very small, unless the light is concentrated. As suggested by Lambarski and Bradwell [2], I_{sc} can be expressed as a function of solar radiation and temperature.

$$I_L = I_{sc} = P_1 G [1 - P_2 (G - G_r) + P_3 (T_p - T_r)] \quad (2)$$

where G = Solar radiation (W/m²), G_r = Reference solar radiation (W/m²), T_r = Reference temperature (K) and P_1, P_2, P_3 = Constants.

Reverse saturation current I_o can be expressed as an exponential function of cell temperature, i.e.

$$I_o = B T_p^3 \left[\exp\left(-\frac{E_{go}}{k T_p} \right) \right] \quad (3)$$

where E_{go} = Band gap energy at 0 K (1.16 eV for silicon) and B = Device and material constant which has to be estimated.

Parameters (or constants) in Eqs. (1), (2) and (3) can be estimated using the information provided by the PV module manufacturer. A typical specification sheet provides I-V characteristics at two different radiation levels. It also gives I-V curves at two or more different cell temperatures. The procedure for the determination of parameters using the above information can be found in Appendix - A.

If all the modules of a PV array are identical, which is the usual case in practice, the I-V curve of the whole array can be determined by scaling the I-V curve of one module, i.e. by multiplying the voltage by the number of modules in series and the current by the number of module strings in parallel.

4. MODEL FOR ESTIMATING PV MODULE TEMPERATURE

The output of a PV module depends on the cell operating temperature. In this study, the cell temperature is considered approximately equal to the PV module temperature, which can be estimated considering the overall energy balance of the PV panel as suggested by Das [3]:

$$(mCp_{module})\frac{dT_p}{dt} = Q_{in} - Q_{rad} - Q_{conv} - Q_{elect} \tag{4}$$

where mCp_{module} = Effective heat capacity of the PV module (J/K), Q_{rad} = Radiative heat loss (W), Q_{conv} = Convective heat loss (W), Q_{elect} = Electrical power produced (W) and Q_{in} = Solar energy absorbed by the module (W).

In heat transfer theory, the radiation heat loss (Q_{rad}) and convective heat loss (Q_{conv}) are given by

$$Q_{rad} = S_p F_{pg} \sigma (E_p T_p^4 - E_g T_g^4) + S_p F_{ps} \sigma (E_p T_p^4 - E_s T_s^4) \tag{5}$$

and

$$Q_{conv} = S_p H (T_p - T_a) \tag{6}$$

where σ = Stephan-Boltzmann constant (56.7×10^{-9} W/m^{2}K^4), F_{pg} = Panel to ground view factor, F_{ps} = Panel to sky view factor, E_p = Average emissivity of panel, E_g = Average emissivity of ground, E_s = Average emissivity of sky, T_g = Ground temperature (= T_a), T_s = Sky temperature (= 0.914 T_a), S_p = Total area of PV module (m^2) and H = Convective heat transfer coefficient (W/m^{2}K).

According to Jet Propulsion Laboratory [4], the convective heat transfer coefficient H can be computed from

$$H = 1.2475 [(T_p - T_a) \cos \beta]^{1/3} + 2.658 v \tag{7}$$

where β = Panel tilt angle (degrees) and v = Wind speed(m/s).

Electrical power produced (Q_{elect}) can be calculated by

$$Q_{elect} = \eta G S_c \tag{8}$$

where η = Module instantaneous efficiency and S_c = Total area of PV cells in a module receiving solar radiation (m^2).

Instantaneous efficiency of the module is expressed as a linear function of module tempera-

ture as suggested by Lasnier et al. [5]:

$$\eta = \eta_o [1 - \gamma (T_p - T_r)] \quad (9)$$

where T_r = Reference temperature (K) and γ = Constant referred as the temperature coefficient of module efficiency.

Energy absorbed by the PV panel is estimated from

$$Q_{in} = \alpha_{abs} G S_c \quad (10)$$

where α_{abs} = overall absorption coefficient.

The value of mCp_{module} and α_{abs} can be determined experimentally and the value of γ can be found using the manufacturer's data as described in Appendix - A. The typical values of the view factors and emissivities can be found in the literature.

5. DESCRIPTION OF THE BATTERY MODEL

Battery model describes the relationship between the voltage, current and state of charge (*SOC*) of the battery. The model used in this study is adopted from the work done by Mayer and Biscaglia [6]. In the model, terminal voltage of a battery is expressed as

$$V_b = E_{oc} + I_b R_b \quad (11)$$

where V_b = Battery terminal voltage (V), E_{oc} = Battery open circuit voltage (V), I_b = Battery current (A) and R_b = Internal resistance of the battery (ohms). The convention used in this study is that I_b is positive when flowing into the battery (i.e. when charging). Both E_{oc} and R_b are dependent on *SOC* of the battery and have different values for charging and discharging modes.

The open circuit voltage, E_{oc}, is expressed as a logarithmic function of battery state of charge (*SOC*):

$$E_{oc} = VF + VS \cdot \log (SOC) \quad (12)$$

where *VF* = Full charge rest voltage (V) and *VS* = Empirical constant (V) which accounts for the variation of open circuit voltage with *SOC*. Both *VF* and *VS* are different for the charging and discharging modes. Hereafter the values of *VF* and *VS* corresponding to charging and discharging modes will be denoted with the subscripts "*c*" and "*d*", respectively.

Battery state of charge, *SOC*, is the instantaneous ratio of actual amount of charge stored in the battery and total charge capacity of the battery at a certain battery current. In the model *SOC* is estimated considering the exchanged charge, as follows:

$$(SOC) = SOC_o + \left[\frac{Q}{BC} \right] \quad (13)$$

where *SOC* = Current State of Charge, SOC_o = Previous State of Charge, Q = Amount of exchanged charge during the interval between the previous time and the current time of interest (C) and *BC* = Battery capacity (C).

Exchanged charge, Q, is determined by summing up of the charge flow over the period of interest, with the convention that any charge flow into the battery is positive.

$$Q = \int_0^t I_b \, dt \tag{14}$$

Battery capacity, BC, of a lead acid battery is a function of the absolute value of battery current, I_b. It is also dependent on the electrolyte temperature. But according to Komp [7], at moderate temperatures, this variation is small1. Therefore the battery capacity in the present model is expressed as a function of battery current only, that is

$$BC = \left[\frac{b_1}{(I_b)^{b_2} + b_3} \right] \tag{15}$$

where b_1, b_2 and b_3 are constant coefficients.

Battery internal resistance, R_b, is considered having two parts, i.e.

$$R_b = R_{electrode} + R_{electrolyte} \tag{16}$$

$R_{electrode}$ and $R_{electrolyte}$ have different values for charging and discharging modes and the following models are used to describe their dependency on the SOC of the battery:

$$R_{electrode} = r_1 + r_2 \, (SOC) \tag{17}$$

and

$$R_{electrolyte} = \left[\frac{1}{r_3 - r_4 \, (SOC)} \right] \tag{18}$$

where r_1, r_2, r_3 and r_4 are empirical constants.

Therefore the total internal resistance of the battery during the charging mode is given by

$$R_c = c_1 + c_2 \, (SOC) + \frac{1}{c_3 - c_4 \, (SOC)} \tag{19}$$

where R_c = Internal resistance during charging (ohms) and c_1 to c_4 are respective values of r_1 to r_4 in Eqs.(17) and (18) for the charging mode.

Similarly the total internal resistance, R_d, during the discharging mode is

$$R_d = d_1 + d_2 \, (SOC) + \frac{1}{d_3 - d_4 \, (SOC)} \tag{20}$$

where d_1 to d_2 are respective values of r_1 to r_4 for the discharging mode.

If it is significant, Equation (13) can be easily modified to accommodate the effect of self discharging, that is

$$SOC = SOC_o + \left[\frac{Q}{BC} \right] - (SDR) \, \delta t \tag{21}$$

where SDR = Self Discharge Rate (C/S) and δt = Time interval of interest (S).

When *SOC* of the battery is reaching close to 100%, the emission of gases occurs; hydrogen at the positive terminal and oxygen at the negative terminal. Although Mayer and Biscaglia [6] have modelled the behavior of batteries when gassing occurs, it is not included in this model due to its additional complexity. On the other hand, the action of the controller prevents overcharging the battery where gas evolution is predominant. Instead it is assumed that a constant factor (5%) of the current entering into the battery is consumed in production of the gases.

Parameters used in the model can be estimated by using the manufacturer's data and the experimental data obtained from charging and discharging tests as explained in Appendix - B.

6. CONTROLLER MODEL

The primary function of the controller in a PV system is the efficient use of photovoltaic energy while providing protection for the expensive batteries. The two main duties of the controller are:

i. Charge regulation, which prevents the over charging of the battery by PV panels.
ii. Discharge regulation, which prevents the excessive discharge of the battery by disconnecting the load under low battery state of charge.

The controller used in the PV refrigeration system under this study was a SCI charger model 1, 12V regulator manufactured by Specialty Concepts Incorporation, U.S.A. It is a negative-ground, series relay regulator with some additional features such as status lights, over load protection and sophisticated float charge mode.

According to the installation and operation manual prepared by Specialty Concepts Inc. [8], the two-step charge control circuit regulates the charging of storage batteries by monitoring the battery and array voltages. When the battery *SOC* is low, e.g. at sunrise, charging relay energizes connecting the PV array directly to the battery. The battery will accept as much current as the array will provide and the battery voltage will rise. This can be called the Full Charge Mode or the Boost Charge Mode (BCM).

When the battery reaches the full charge termination threshold, charging relay will open. At this point the float charge regulator takes over the control. The operation of regulator in Float Charge Mode (FCM) is such that, it keeps the battery voltage below the Maximum Float Voltage (MFV) and limits current to the Maximum Float Current (MFC). As the battery approaches the float voltage, the current ceases thus preventing further charging of battery.

If a load is applied when the charger is in the boost charge mode and if the array current is greater than the load demand, the rest is used for charging the battery. On the other hand, if the array current is less than the load demand, the battery will supply the balance.

If a load is applied when the charger is in the float charge mode, the regulator will supply up to its maximum float current to maintain the battery charge. If the load is more than the maximum float current, the battery will still be receiving a net charge from the float regulator. If the load current is more than the maximum float current, the battery will supply what the float regulator cannot and the battery voltage will fall. When it falls below the full charge resumption threshold, the charging relay will re-close, re-initiating the boost charge mode.

The Low Voltage Disconnect (LVD) mode of the regulator prevents the battery from being over-discharged by disconnecting the load whenever the battery voltage goes below the low voltage disconnect threshold. Load will be re-connected when the battery voltage reaches Load Re-connect Threshold (LRT). Table 1 gives the ratings and threshold voltages for the SCI charger model 1.

Table 1. The ratings and thresholds for SCI charger model-1.

Parameter	Unit	Value
Nominal Voltage	V	12
Charge Current (max)	A	30
Load Current (max)	A	30
Operating Temperature	°C	0 - 50
Current Consumption (charging)	A	0.16
Current Consumption (load disconnect)	A	0.14
Quiescent Current	A	0.01
Full Charge Termination	V	14.8 ± 0.2
Full Charge Resumption	V	12.5 ± 0.2
Low Voltage Disconnect	V	11.5 ± 0.5
Load Reconnect	V	13.0 ± 0.3
Max. Float Voltage	V	14.1 ± 0.2
Max. Float Current	A	3.0

Given an array current and a load demand (i.e. current demand from the compressors), a controller model must be able to determine the battery current corresponding to the existing state of charge of the battery (which corresponds to the battery voltage) and various set thresholds of the controller. For the purpose of modelling the controller, the following logical variables were introduced:

BCM equals "1" whenever the charger is operating in boost (or full) charge mode. Otherwise it is "0".

LVD equals "1" whenever the load is disconnected due to the operation of low voltage disconnect relay. Otherwise it is "0".

MFV equals "1" whenever the battery exceeds the maximum float voltage, provided that the charger is operating in float charge mode. Otherwise it is "0".

MFC equals "1" whenever the array current exceeds the maximum float current, provided that the charger is operating in the float charge mode. Otherwise it is "0".

With the help of the above logical variables, the battery current can be expressed as

$$I_b = I_p\,(BCM) + \{\,3\,(MFC) + I_p\,[\,1-(MFC)\,]\,\}\,[\,1-(MFV)\,]\,[\,1-(BCM)\,] - [\,1-(LVD)\,]\,(I_r + I_f) - 0.14\,(LVD) - 0.16\,(BCM) - 0.01 \qquad (22)$$

where I_b= Battery current (A), I_r= Current demanded by the compressor for refrigerator (A), I_f= Current demanded by the compressor for freezer (A) and I_p= Current provided by the PV panel (A).

The values '0.14' and '0.16' in Eq.(22) represent the current consumption of the relays during low voltage disconnect and full charge mode, respectively. The value '3' is the maximum float current and '0.01' is the current consumption of the controller electronics.

7. THEORETICAL MODEL OF THE REFRIGERATOR

The SHOWA ARCO model SASFE refrigerator used for this study contains two separate compartments: one for vaccine storage and the other for ice-pack freezing. The freezer compartment has a thicker insulation cover than the vaccine storage compartment. In addition to the common door at the top side of the cabinet, there is a second separate insulation lid for the freezer compartment. Also it has two refrigeration circuits and each compartment is cooled by the operation of its own compressor unit. Two hermetically sealed DANFOSS model BD2.5 piston compressors operate on 12 V dc supply. Each compressor, which uses a brushless dc motor, is provided with an electronic commutation unit accompanying overload and under voltage protection. Two condensers corresponding to the two refrigeration circuits are skin type and attached to either side of the cabinet. The temperature of each chamber can be selected independently through the two thermostats provided. The refrigerant used is R-12. Throttling is achieved passing the high pressure liquid through capillary tubes. Figure 2 shows a sketch of the SHOWA ARCO model SASFE PV refrigerator.

The cooling effect of a refrigerator is produced through the absorption of heat at a lower temperature by the evaporator coils. In modelling the refrigerator, the net cooling output of the system, i.e. extraction of heat from the refrigerator cabinet, can be related to the electrical energy input to the compressor through the coefficient of performance (*COP*) of the refrigerator. If the heat extracted in an elementary time interval, δt, is equal to δQ_{ext} and the rate of electrical energy input to the compressors is P, the relationship can be mathematically expressed as

$$\delta Q_{ext} = (COP) . P . \delta t \tag{23}$$

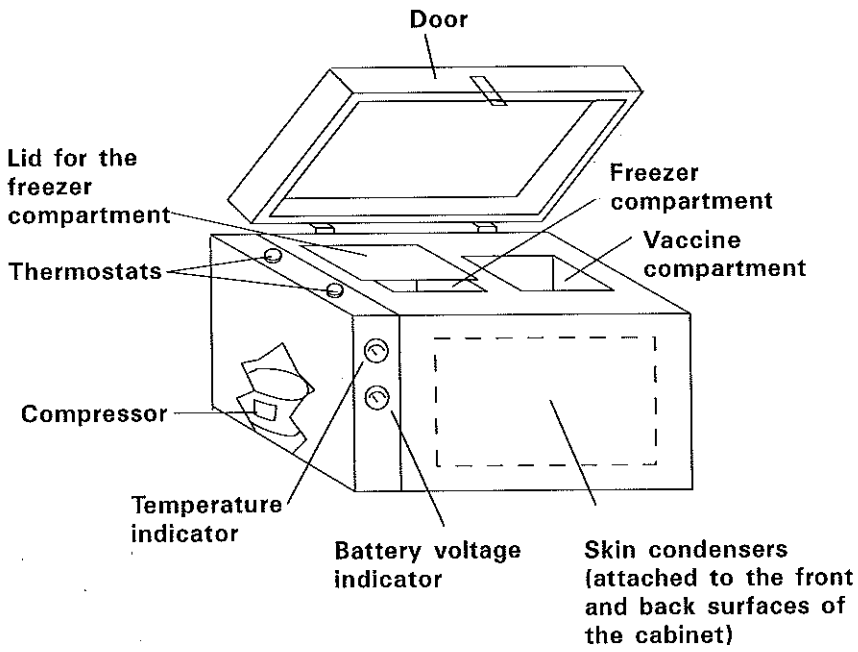

Fig. 2. SHOWA ARCO model SASFE refrigerator.

This absorbed heat, together with the energy supplied to the compressor, is rejected to the high temperature surrounding at the condenser. Therefore the heat rejected, δQ_{rej}, at the condenser in the time interval δt, can be expressed as

$$\delta Q_{rej} = (1 + COP) . P . \delta t \quad (24)$$

A preliminary investigation was carried out on the refrigerator before modelling, in order to understand the temperature distribution and the heat transfer processes inside the refrigerator cabinet. The observations made are:

(a) Walls of the vaccine storage chamber and the freezer chamber operate at different temperatures which can be controlled independently. Also, these temperatures are very close to the evaporator temperatures of the respective refrigeration circuits.
(b) At stable running state, the average temperature of the ice-packs is almost equal to the average freezer compartment wall temperature.
(c) At stable running state, the average temperature of the vaccine load is slightly higher than that of the refrigeration compartment wall.
(d) The temperature at the outer surface of either wall where the skin condenser is located, rises above the ambient temperature when the corresponding compressor is working.

According to the above observations, the refrigerator cabinet containing ice-packs and vaccine load can be represented by six lumped heat capacitances:

mC_{pwr}, the effective heat capacity of all components surrounding the vaccine storage compartment (which will be hereafter referred to as "refrigerator wall"), expressed with respect to the temperature at the inner side of the wall.
mC_{pwf}, the effective heat capacity of all components surrounding the freezer compartment (which will be hereafter referred to as "freezer wall"), expressed with respect to the temperature at the inner side of the freezer wall.
mC_{pvl}, the effective heat capacity of the vaccine load expressed with respect to the temperature at the middle of the vaccine load.
mC_{pip}, the heat capacity of the ice-packs, which is approximately the heat capacity of water or ice contained in the ice packs.
mC_{pcr}, the effective heat capacity of the condenser for vaccine storage compartment refrigeration circuit.
mC_{pcf}, the effective heat capacity of the condenser for freezer refrigeration circuit.

The heat transfer network shown in Fig. 3a can be developed to describe the heat transfer processes among these heat capacitances. Absorptions of heat by the two evaporator coils embedded in the cabinet wall are represented by two heat sinks located at the refrigerator and freezer walls. Heat rejections by the two condensers are represented by two heat sources located at the nodes corresponding to two condensers.

Although the above heat transfer network gives a complete representation of the refrigerator, it is too complex and evaluation of the various heat transfer coefficients and heat capacities would be a tedious task requiring a number of sophisticated tests, which in turn reduce the practical use of the model. The added complexity is mainly introduced by the heat transfer links between the walls and the condensers.

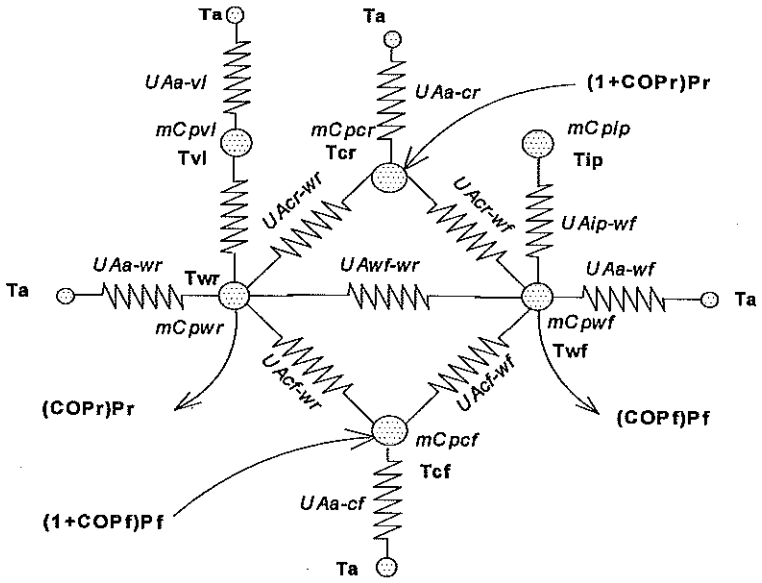

Fig. 3(a). Complete heat transfer network for the refrigerator model.

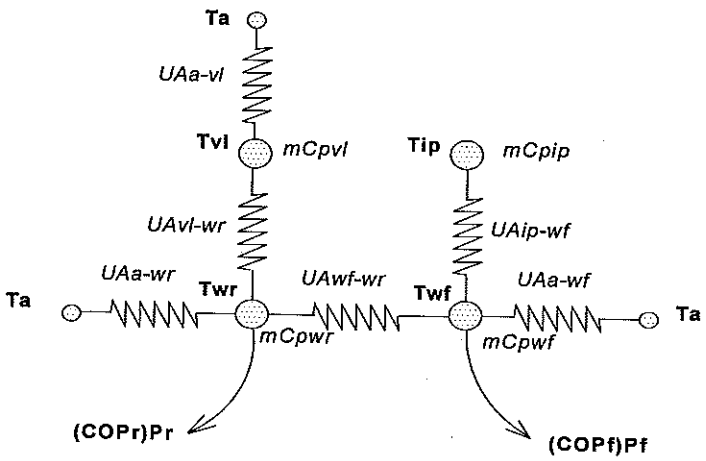

Fig. 3(b). Simplified heat transfer network for the refrigerator model.

Furthermore, the average effect of the condensers is in one way equivalent to the increasing of apparent ambient temperature, which in turn increases the heat gain to the refrigerator cabinet. Therefore, even when the links between condensers and walls are neglected, the average effect of the skin condensers would be represented by off-setting the values of heat transfer coefficients between the walls and the ambience.

Therefore, it was decided to neglect the effect of skin condensers in order to avoid the added complexity, on the assumption that the design of the cabinet is such that most of the heat rejected at the condensers is dissipated to the ambience, allowing only a negligible amount of heat to flow back into the cabinet. Under this assumption, the heat transfer network can be simplified as shown in Fig.3b. Considering the heat balance at each of the nodes, the following differential equations can be established:

$$m\,C_{pwr}\frac{dT_{wr}}{dt} = U\,A_{vl-wr}(T_{vl}-T_{wr}) + U\,A_{a-wr}(T_a-T_{wr}) + U\,A_{wf-wr}(T_{wf}-T_{wr}) - (COP_r)\,P_r \quad (25)$$

$$m\,C_{pwf}\frac{dT_{wf}}{dt} = U\,A_{ip-wf}(T_{ip}-T_{wf}) + U\,A_{a-wf}(T_a-T_{wf}) + U\,A_{wf-wr}(T_{wr}-T_{wf}) - (COP_f)\,P_f \quad (26)$$

$$m\,C_{pvl}\frac{dT_{vl}}{dt} = U\,A_{a-vl}(T_a-T_{vl}) + U\,A_{vl-wr}(T_{wr}-T_{vl}) \quad (27)$$

If $T_{ip} > 0$°C,

$$m_{ip}\,C_{pw}\frac{dT_{ip}}{dt} = U\,A_{ip-wf}(T_{wf}-T_{ip}) \quad (28)$$

If $T_{ip} < 0$°C,

$$m_{ip}\,C_{pi}\frac{dT_{ip}}{dt} = U\,A_{ip-wf}(T_{wf}-T_{ip}) \quad (29)$$

If $T_{ip} = 0$°C,

$$P_{latent} = U\,A_{ip-wf}(T_{ip}-T_{wf}) \quad (30)$$

and T_{ip} remains unchanged until

$$\int P_{latent}\,dt = m_{ip}\,L \quad (31)$$

Note that UA_{a-wr} = Heat transfer coefficient between the refrigerator wall and the ambience (W/K), UA_{a-wf} = Heat transfer coefficient between the freezer wall and the ambience (W/K), UA_{vl-wr} = Heat transfer coefficient between the refrigerator wall and the vaccine load (W/K), UA_{ip-wf} = Heat transfer coefficient between the freezer wall and the ice-packs (W/K), UA_{a-vl} = Heat transfer coefficient between the vaccine load and the ambience (W/K), UA_{wf-wr} = Heat transfer coefficient between the freezer wall and the refrigerator wall (W/K), mC_{pwr} = Heat capacity of the refrigerator wall (J/K), mC_{pwf} = Heat capacity of the freezer wall (J/K), mC_{pvl} = Heat capacity of the vaccine load (J/K), C_{pw} = Specific heat capacity of water (J/kg K), C_{pi} = Specific heat capacity of ice (J/kg K), m_{ip} = Mass of ice-packs (kg), L = Specific latent heat of fusion (J/kg), P_{latent} = Rate of release of latent heat of fusion (W), P_r = Power supplied to the compressor for vaccine chamber(W), P_f = Power supplied to

the compressor for freezer (W), COP_r = *COP* of the refrigeration circuit for vaccine chamber, COP_f = *COP* of the refrigeration circuit for freezer, and T_{wr}, T_{wf}, T_{vl}, T_{ip}, T_a are the temperatures at the refrigerator wall, freezer wall, vaccine load, ice-packs, and ambience, respectively.

Six heat transfer coefficients and four heat capacities in the heat transfer network can be determined through a series of tests performed on the refrigerator under a controlled environment, as described in Appendix - C.

Kilfoyle et al. [9] carried out a study on the long term performance of PV vaccine refrigerators and found that the *COP* of the PV refrigerators has a value around 1.0, which slightly varies with the ambient temperature. The study was based on three refrigerators; MARVAL model 4STD, SUNFROST model RFV4 and POLAR PROD. model RR2. The third refrigerator had the same configuration as SHOWA ARCO model SASFE, with double compressors. According to their estimations the average COP of the three systems were equal to 1.0, 1.5 and 1.0, respectively. Furthermore, they modeled the COP of the first and the third systems as linear functions of ambient temperature:

$$COP_1 = 1.10\,(1.0 + 0.015\,(30 - T_a)) \tag{32}$$

$$COP_3 = 1.11\,(1.0 + 0.010\,(30 - T_a)) \tag{33}$$

Accordingly, the *COP* of the first refrigerator changes from 1.35 to 0.89 in the ambient temperature range from 15°C to 43°C. The *COP* change of the third refrigerator for the same temperature range is from 1.28 to 0.97. From the DANFOSS spec sheet [10], an approximate value for the *COP* of SHOWA ARCO refrigerator can be found. According to the specifications given for BD2.5 compressor at 32°C, for the evaporator temperature range between -20°C and -10°C, *COP* lies between 0.915 and 1.15. Both the refrigeration circuits in the SHOWA ARCO model SASFE refrigerator use DANFOSS model BD2.5 compressors. Therefore, based on the findings by Kilfoyle et al. [9] and the information in DANFOSS specification sheet, it is assumed that 1.0 is the typical value of *COP* for both refrigeration circuits (i.e. $COP_r = COP_f = 1.0$) and the variation of the *COP* is considered small within the interested ambient temperature range from 15°C to 43°C.

It was found that the *UA* values in the Eq.(25) to Eq.(31) are temperature dependent according to Charters and Aye [11] and Bato-on [12]. This is mainly due to the temperature dependence of thermal conductivity of the polyurethene foam, which is used as the insulation material in walls. They have used different models to describe the temperature dependency of the thermal conductivity of insulation materials. Charters and Aye [11] modeled the overall heat transfer coefficient of a refrigerator as a linear function of the mean temperature of the cabinet wall while Bato-on [12] expressed the heat transfer coefficient between the ambience and the cabinet wall as a cubic function of ambient temperature.

However, the variations of *UA* values with the ambient temperature cannot be completely imputed to the variation of thermal conductivity of polyurethene foam. The effects of the skin condensers may have been reflected in these parameters. Also, possible reduction of *COP* at high ambient temperatures can appear in the model in the form of increased heat transfer coefficients. Furthermore, these heat transfer coefficients represent not only the heat transfer through the wall insulation, but also the heat transfer between ambient air and cabinet surface, part of which is through the radiation.

In this study, UA_{a-wr}, UA_{a-wf} and UA_{a-vl} are modeled as the functions of ambient temperature (T_a), rather than functions of mean temperature of the cabinet wall. The following fourth order

expression is used to establish the relationship between the heat transfer coefficients and ambient temperature. For example,

$$U A_{a-wr} = U_o + U_1 T_a^3 + U_2 T_a^4 \quad (34)$$

where U_0, U_1 and U_2 are constants to be found from experimental tests.

Since the variations of the averages of T_{vl}, T_{wr}, T_{wf} and T_{ip} with the ambient temperature at a stable running state are very small, it is assumed that UA_{vl-wr}, UA_{ip-wf} and UA_{wf-wr} are constants.

Heat capacities of the refrigerator wall and freezer wall, which were calculated using the above ambient temperature dependent heat transfer coefficients also vary with the ambient temperature. Therefore, a similar fourth order expression is used for representing the ambient temperature dependencies of mC_{pwr} and mC_{pwf}. For example,

$$m C_{pwr} = C_o + C_1 T_a^3 + C_2 T_a^4 \quad (35)$$

where C_0, C_1 and C_2 are constants to be found from experimental tests.

8. EXPERIMENTAL VERIFICATION OF THE SIMULATION MODEL

In experimental verification of the PV refrigeration system simulation model developed, the actual PV refrigeration system was first run under natural conditions while recording the information on the system performance (temperatures, currents and voltages) as well as the prevailing meteorological conditions (solar radiation, outside ambient temperature and room temperature). Then the gathered data on the meteorological conditions during the test run was fed into the computer program written linking the four mathematical models discussed previously and the predicted system performance was compared against the measurements on the actual system.

The test run of the PV refrigeration system was carried out in the Energy Park of the Asian Institute of Technology, Bangkok, Thailand, where the PV refrigeration system under this study was installed. The experimental set-up consisted of an extensive data acquisition system in order to measure and record, every five minutes, the required information on the system and the meteorological conditions. The test run was started on June 3,1993 and extended for 10 days. In order to investigate the model's ability to predict the system performance under different operating conditions, this test run was divided into 7 phases as follows:

Phase-1: At the beginning of Phase-1, refrigerator cabinet, vaccine load and ice-packs (1.8kg) were stabilized at ambient temperature. Battery was at fully charged condition (SOC=100%). Only the refrigerator was switched on at the start of Phase-1.

Phase-2: Refrigerator compartment had already cooled down in Phase-1 and operating within its steady state temperature range. At the beginning of Phase-2, the freezer compressor was also switched on. This phase was extended until all the ice-packs were frozen and the freezer compressor initiated its intermittent operating cycle .

Phase-3: During this phase the battery state of charge dropped below the low voltage cut-off level. Load disconnection occurred after midnight (around 04:30 hrs) and load was reconnected the following morning. Both compressors were switched on throughout the period.

Phase-4: Both refrigerator and freezer were in steady operation. All the ice-packs were frozen.

Phase-5: At the beginning of Phase-5, the freezer compressor was switched off, but the refrigerator compressor continued its operation. The frozen ice-packs slowly melted.

This phase was extended until all ice-packs became water.

Phase-6: At the end of Phase-5, all melted ice-packs were removed. Then the freezer compressor switched on without ice-packs (no load) while the refrigerator was still in its usual operation.

Phase-7: Ice-packs (1.8kg) at ambient temperature were reloaded into the already cooled freezer compartment while both compressors were still in operation.

9. DISCUSSION OF EXPERIMENTAL RESULTS

The above 7 phases were carefully selected to critically test the effects of each individual component model on the simulation model's ability to predict the performance under different operating conditions. Note that, it is not intended to discuss the performance in all 7 phases in this paper, as it would be too long. Instead, validity of component models will be discussed with selected examples.

The variation of the global solar radiation on the panel in the first day in Phase-1 is given in Fig. 4. At noon the radiation level rises over 1100 W/m^2 but in the afternoon, the radiation is low. Figure 5 shows the variation of array current on that day. According to this figure, the predicted and observed variations agree well, except at one instant where the computed current is lower than the measured one. This point corresponds to the peak in radiation level. On the other hand, corresponding to the valley in solar radiation variation shown in Fig. 4, the predicted array current is slightly higher than the actual. These suggest that the differences between predicted and ob-

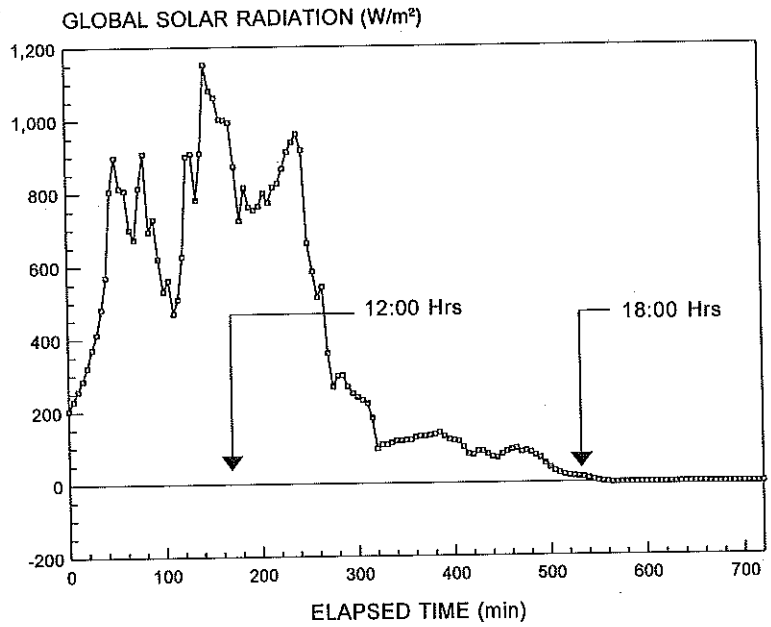

Fig. 4. Variation of global solar radiation on a plane tilted 15° to the south.

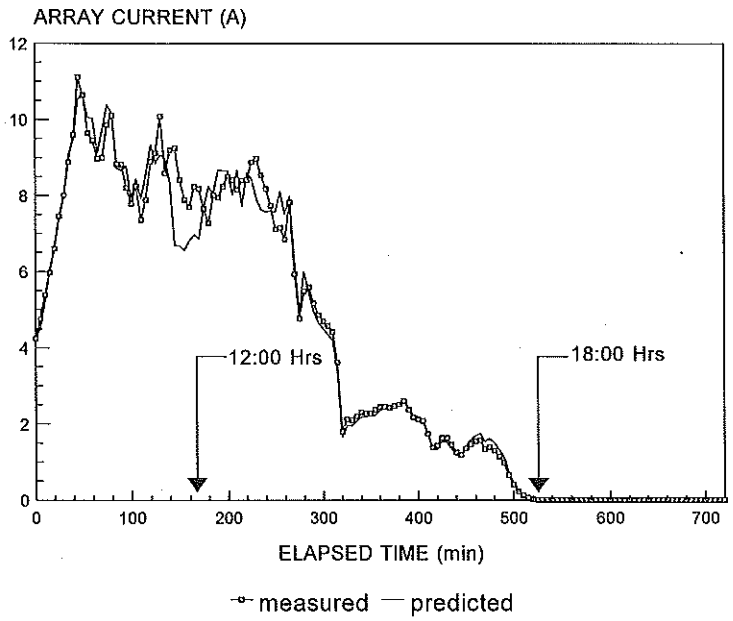

Fig. 5. Comparison of the predicted and measured variations of PV array current.

served current come from the over-sensitivity of the panel temperature model to the changes in solar radiation. The response of the panel temperature model is faster than the actual. Therefore at the sudden peak of radiation, the predicted array temperature is higher than that of actual. This has resulted in a lower predicted current at the peak radiation. When the radiation level drops sharply, the predicted panel temperature drops faster than the actual panel temperature, resulting in higher predicted current than the observed one.

It can be noticed that, at the peak radiation, both predicted and actual array currents are lower than the currents observed during lower radiation levels in the morning. There are two reasons for this: reduction of open circuit voltage due to high cell temperature and increased battery voltage after charging throughout the morning. This observation emphasizes the importance of using a model which considers the interaction between the battery and PV array.

The variations of battery current and voltage during this period are shown in Figs. 6 and 7. The differences in the computed and measured currents come from the shift between the predicted and actual compressor ON times. Deviations which occurred in the array current prediction are also reflected in the battery current variation. In addition to the error due to the shift in compressor ON times, the prediction of battery voltage deviates slightly from the actual variation. According to the model, the battery has two different open circuit voltages in charging and discharging modes. Corresponding change in the open circuit voltage (when changing the mode from charging to discharging or vice versa) is abrupt. Whereas in the actual battery, this is gradual, specially when the currents are small. Also in the night (when there is no array current) the controller draws a small current from the battery. Hence the open circuit voltage of the battery is corresponding to the discharge mode, which is lower than that in the charging mode. But in the actual case, battery open circuit voltage does not vary much from its value in the charging mode, when discharging at very low currents. This implies that the battery model is less accurate at very small currents.

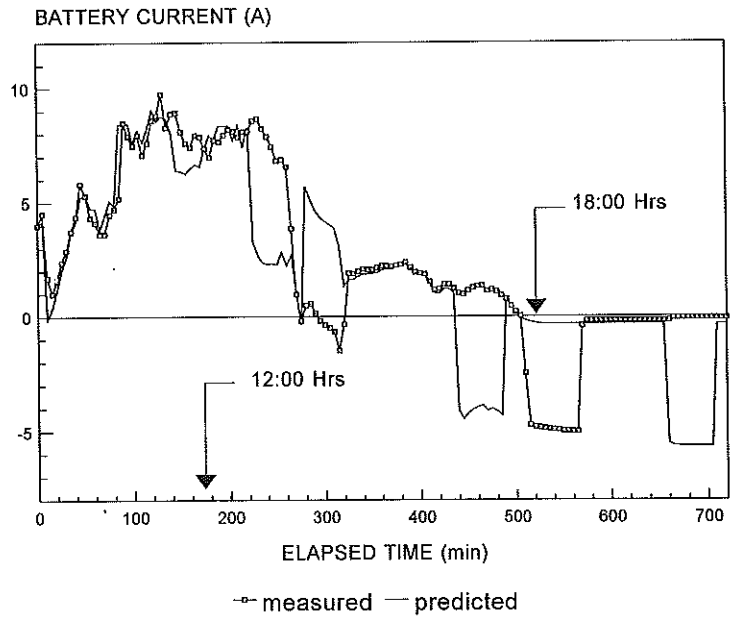

Fig. 6. Comparison of the predicted and measured variations of battery current.

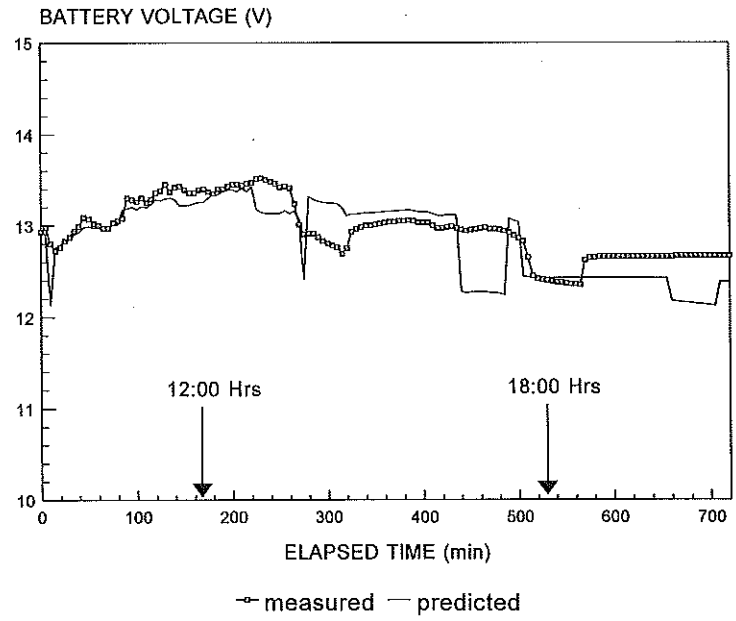

Fig. 7. Comparison of the predicted and measured variations of battery voltage.

In Figs. 8 and 9, the predicted and observed refrigerator performance in Phase-4, during which both compressors were under stable operation, are compared. Good agreement between predicted and observed temperatures can be seen in Phase-4, except for the differences in the period of the operating cycle. For example, the observed period of the cycle is about 15-20 minutes longer than that of the predicted, for the refrigerator compressor. This difference could be seen throughout all 7 phases. As a result, the predicted energy consumptions in Phase-4 are 16.9% and 20.8% lower than the actual energy consumptions for refrigerator and freezer compressors, respectively (Table 2).

Table 2. Comparison of energy consumptions of refrigerator and freezer compressors for various operating conditions.

Phase No.	Duration (hours)	Energy consumed by refrigerator compressor (Wh)			Energy consumed by freezer compressor (Wh)		
		Actual	Predicted	% Diff	Actual	Predicted	% Diff
Phase -1	25.0	573.0	522.8	8.7	–	–	–
Phase -2	36.0	535.4	431.0	19.5	2000.0	762.7	61.8
Phase -3	18.8	209.0	183.9	12.0	277.4	222.5	19.8
Phase -4	12.0	174.0	144.6	16.9	209.5	165.8	20.8
Phase -5	49.5	729.6	715.3	1.9	–	–	–
Phase -6	22.6	280.8	280.8	0.0	387.3	312.6	19.3
Phase -7	18.0	182.0	184.1	-1.1	804.1	436.4	45.7

Note : % Diff = % difference of predicted value from the actual value.

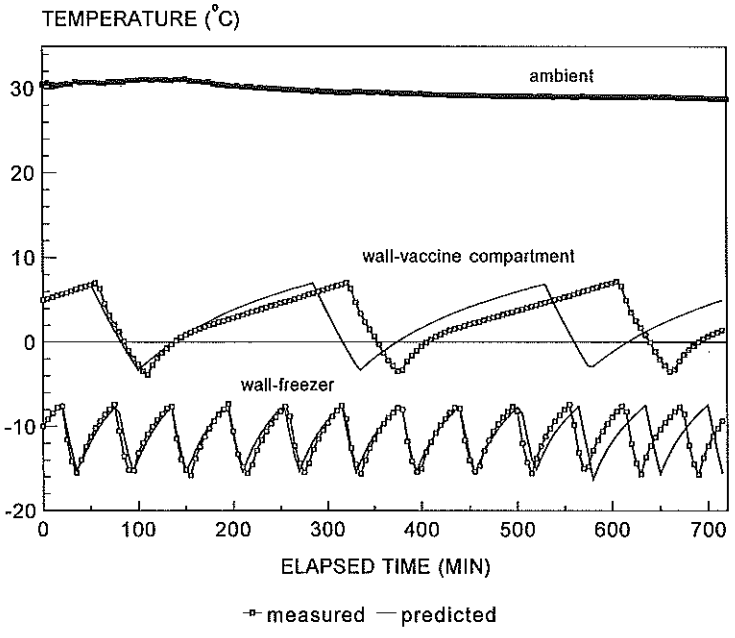

Fig. 8. Comparison of the predicted and measured variations of refrigerator and freezer wall temperatures in Phase-4.

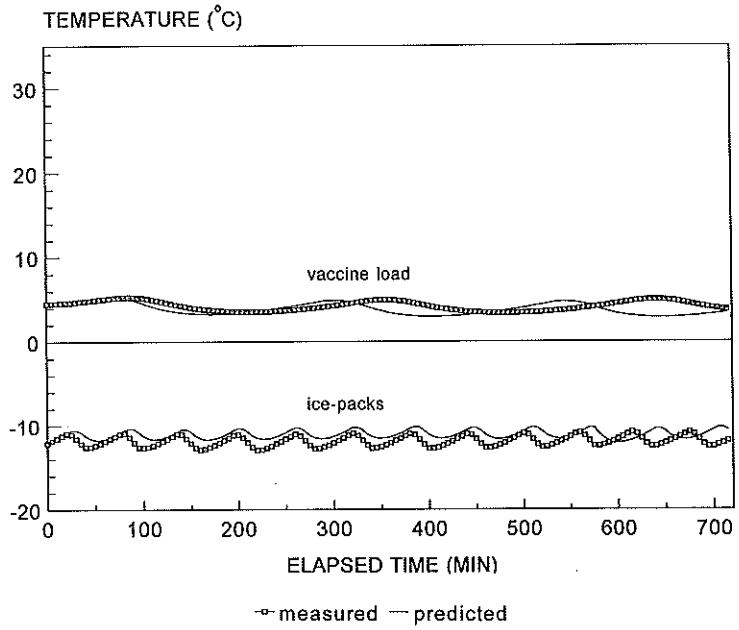

Fig. 9. Comparison of the predicted and measured variations of vaccine load and ice-pack temperatures in Phase-4.

The parameter which directly influences on the periodic time of the refrigerator compressor running cycle is the heat capacity of the refrigerator wall, mC_{pwr}. This parameter is ambient temperature dependent and the variation with ambient temperature was established by the exact fitting of three mC_{pwr} values estimated at 15°C, 32°C and 43°C, into Eq.(35). The fitting is shown in Fig. 10. There is a sharp rise in mC_{pwr} in the ambient temperature range between 32°C and 43°C whereas the rise of mC_{pwr} in the range from 15°C to 32°C is only marginal. These extreme situations have forced the fitted curve to have a sag between 15°C and 32°C (Fig.10). Due to this sag, some values of mC_{pwr} in between 15°C and 32°C, are lower than the value of mC_{pwr} at 15°C, which should actually increase with the temperature. This sagging nature of the curve has resulted in a lower mC_{pwr} corresponding to the conditions of test run, where the average ambient temperature was 29°C. The influence of low mC_{pwr} is to reduce both ON and OFF periods of the refrigerator compressor running cycle.

Figures 11 and 12 show the predicted and actual temperature variations in Phase-2. According to the predicted performance, the freezer compressor starts its stable operation (cycling) 2 hours after the start. But during the test run, the freezer compressor operated continuously for 34 hours prior to beginning the stable operation (Fig. 11). The observed variation of the ice-pack temperature differs from the predicted (Fig. 12) due to the super cooling. According to Table 2, the predicted power consumption is 61.8% less than the actual power consumption due to the continuous operation of the freezer compressor over a long period.

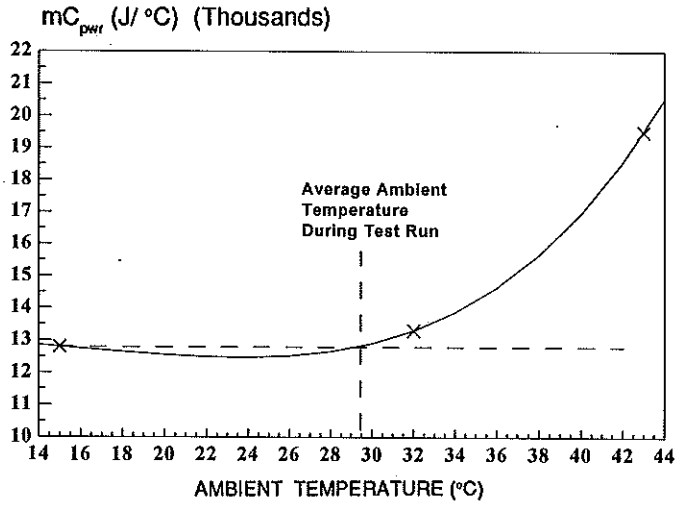

Fig. 10. Sag in the curve fitted for mC_{pwr}.

During the tests performed for estimation of refrigerator model parameters it was noticed that at 43°C, the freezer wall temperature never reached the cut-off limit. At 32°C, the freezer compressor took a very long time to bring down the freezer wall temperature to the cut-off limit (39 hours). Once it reached the cut-off limit it could continue normal cyclic operation. This indicated that the performance of the refrigerator is weakening when the ambient temperature increases. This happens, not only due to the increased heat gain from the surroundings, but also due to the reduction of effectiveness of the refrigeration circuits. At high ambient temperatures, the amount of heat that skin condensers can dissipate to the surroundings becomes less and more heat tends to flow back into the refrigerator cabinet. To remove this heat, compressors have to run more. Continued operation of the compressors causes skin condensers to attain higher temperatures allowing a substantial amount of heat to flow back into the cabinet. The above behavior during the transient periods could not be accurately simulated due to the omission of skin condensers in the simplified heat transfer network.

However, those effects appear in the model in another form as increased heat transfer coefficients at high ambient temperatures. The values of UA_{a-wr} and UA_{a-wf} estimated at 15°C and 32°C were small (with a slightly higher value corresponding to 32°C) compared to the values of those at 43°C. The effect is dominant in the freezer, which operates about 10°C below the refrigerator. Heat capacities were estimated using the above computed values of heat transfer coefficients. Therefore, the above sharp rises of UA_{a-wr} and UA_{a-wf} are reflected in the heat capacities of freezer and refrigerator walls too. On the other hand, only the stable period was considered in estimation of heat transfer coefficients, the effects of skin condensers which are more dominant during the initial cool down period are not included in them (The exception is at 43°C ambient where the freezer compressor runs non-stop). As a result, the prediction of the refrigerator performance during the ice-packs freezing is not accurate.

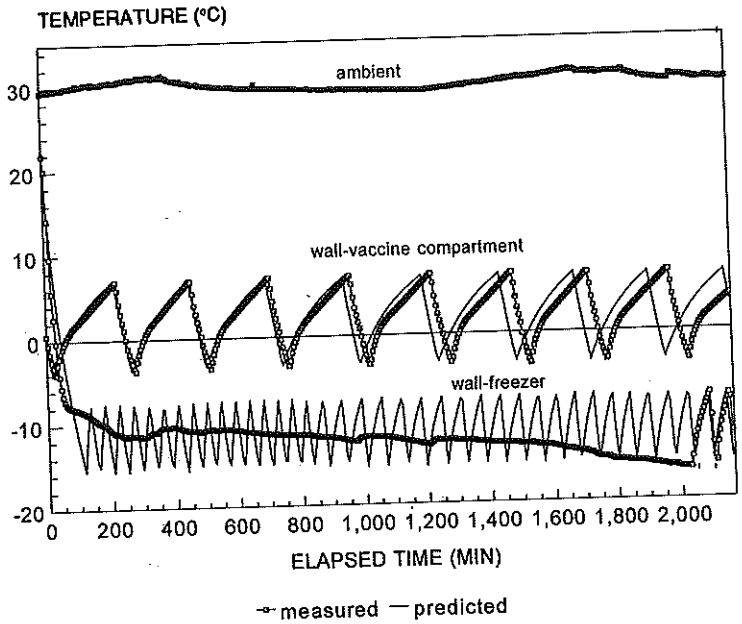

Fig. 11. Comparison of the predicted and measured variations of refrigerator and freezer wall temperatures in Phase-2.

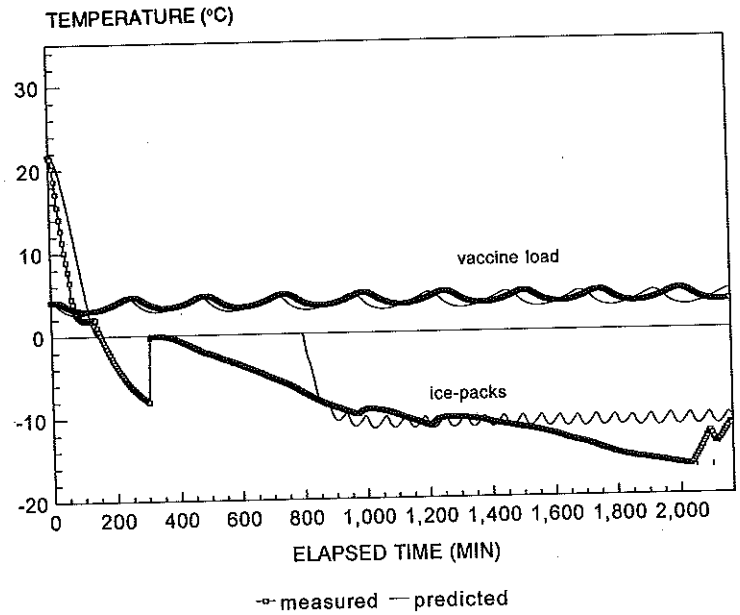

Fig. 12. Comparison of the predicted and measured variations of vaccine load and ice-pack temperatures in Phase-2.

Figures 13 and 14 show the variations of T_{wr}, T_{wf}, T_{vl} and T_{ip}, when the freezer is switched off after freezing ice-packs (Phase- 5). There is a close resemblance between the actual and predicted variations of ice-pack and freezer wall temperatures. During the entire period of phase change (from ice to water), the predicted temperature is held at 0°C, exactly according to the theoretical model. But measured ice-pack temperature increases slowly during this period, after staying at 0°C for a short time. This is because, all the ice-packs in the freezer compartment are not undergoing the phase change exactly at the same time. Temperatures of some ice-packs tends to go up absorbing heat from the freezer wall, while others are still melting. Therefore, the time taken for the complete phase change has been extended in the actual situation.

After prolonged operation of the freezer compressor, the state of charge of the battery was very low at the end of Phase-2. Subsequently, a low voltage disconnection occurred in Phase-3. Figures 15 and 16 show the battery voltage and battery current variations during this period. When compared with the predicted performance, there is a time difference between the actual and predicted activations of low voltage disconnection. But it can be seen that, in both variations of battery voltage, the drop of voltage below the low voltage disconnect threshold coincides with the simultaneous operation of two compressors. The time difference is due to the shift in compressor ON times.

According to the observed results, the load is reconnected about 80 minutes after the sun rise, when the array current is about 4.5A. At that time, the battery voltage is about 12.75V, which is 0.25 volts lower than the load re-connection threshold. But this lies in the range specified by the manufacturer, which is 13.0±0.5V. In the predicted variation of battery voltage, the load re-connection occurs exactly at 13.0V, about 30 minutes later than the observed load re-connection.

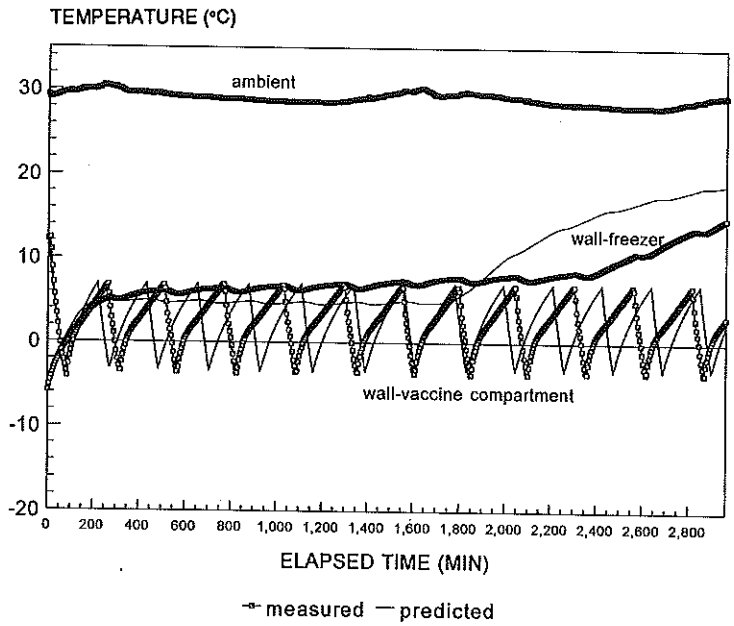

Fig. 13. Comparison of the predicted and measured variations of refrigerator and freezer wall temperatures in Phase-5.

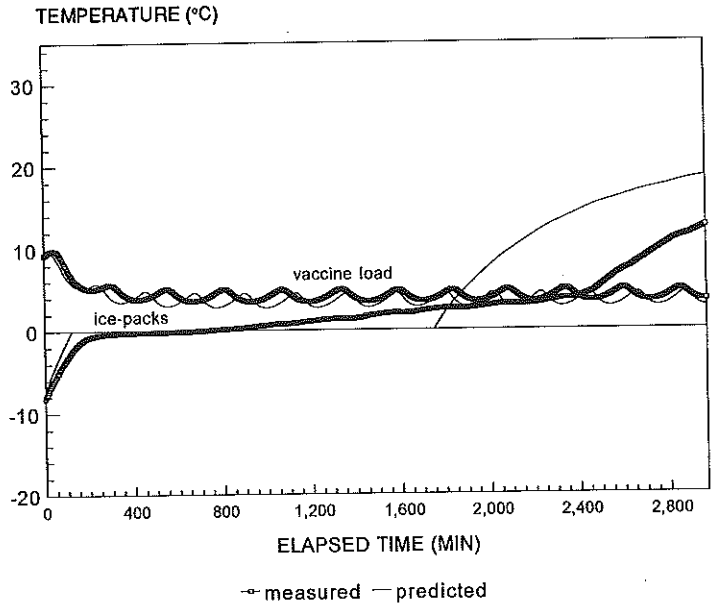

Fig. 14. Comparison of the predicted and measured variations of vaccine load and ice-pack temperatures in Phase-5.

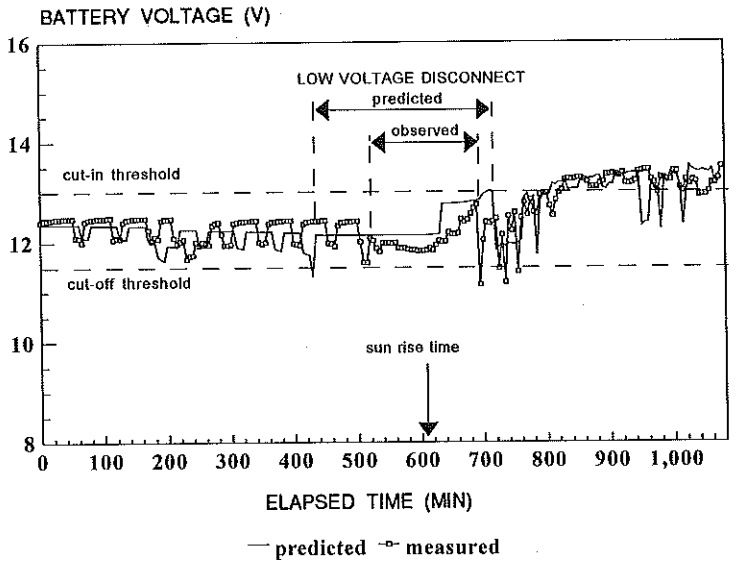

Fig. 15. Comparison of the predicted and measured variations of battery voltage during the low voltage disconnection.

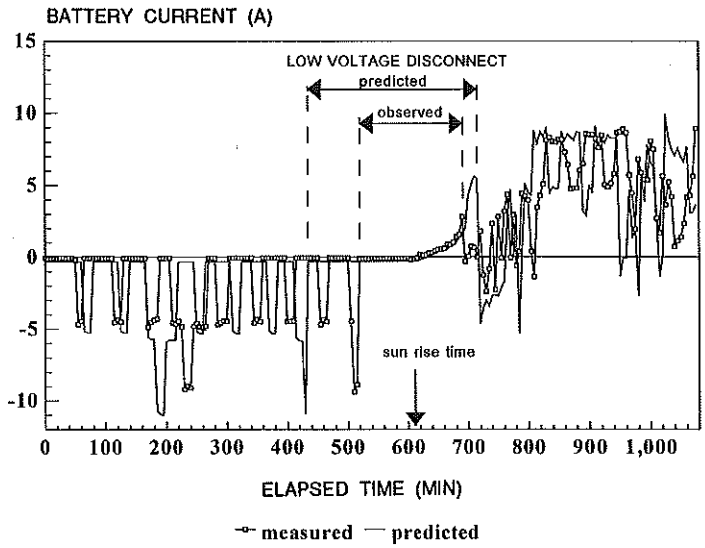

Fig. 16. Comparison of the predicted and measured variations of battery current during the low voltage disconnection.

Figure 17 shows the variations of T_{vl} and T_{ip} during this period. Since the predicted duration of the low voltage disconnection is longer than the observed duration, the predicted temperature elevations are higher than the observed. It can be noticed from Fig. 17 that the temperature of the vaccine load rises slightly above 8°C, which is the recommended maximum safe temperature for vaccine, for a short period (130 minutes in the predicted case and 80 minutes for actual operation).

10. CONCLUSION

In this paper, a simulation model for a stand-alone PV refrigeration system is described in detail and the results of the experimental investigation carried out on a vaccine refrigeration system in order to test the validity of the simulation model are presented.

According to the experimental results, the predicted PV array performance agreed well with the experimental observations, except at the sudden peaks and valleys of global solar radiation where the inaccuracy of panel temperature prediction introduces a small error. The prediction of battery current showed a good agreement with the experimental observations. The prediction of battery voltage was satisfactory, but deviated from the actual values at some instances. However, the battery model suffered from the limited capability in prediction of performance at very low currents and transients. Based on the results obtained with a selected refrigerator, the refrigerator model was not fully capable of predicting the instantaneous temperatures at the refrigerator wall, freezer wall, vaccine load and ice-packs accurately, although it could predict close averages during the stable running periods. Instantaneous wall temperatures of the refrigerator and freezer are the

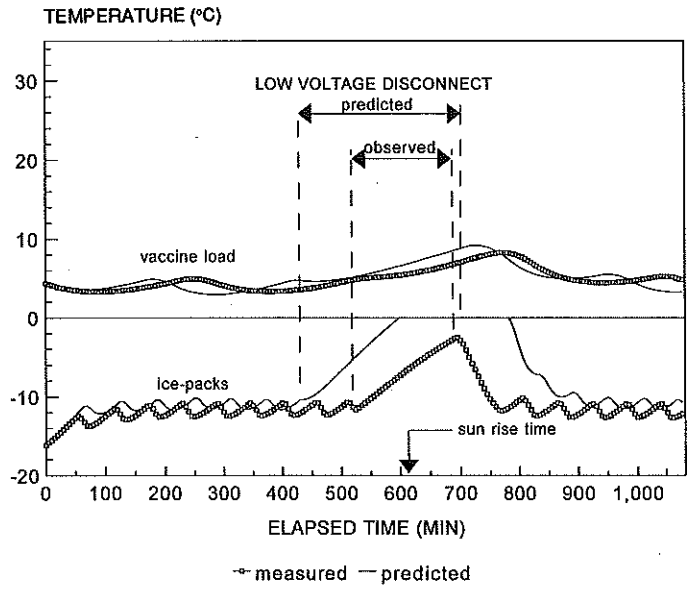

Fig. 17. Comparison of the predicted and measured variations of vaccine load and ice-pack temperatures during the low voltage disconnection.

factors which control the cut-in and cut-off points of the compressors, hence the prediction of power consumption. Inaccurate prediction of instantaneous wall temperatures introduced considerable error in the predicted energy consumption.

The major cause for most of the inaccuracies in the refrigerator performance prediction arose from the exclusion of skin condensers from the simplified refrigerator model. However, the above model may be successfully used with refrigerators which do not have skin condensers.

This paper attempts to detail out all the problems and shortcomings encountered in the existing model along with proposed solutions so that they will be taken into account in future developments or improvements of the simulation model. If the model can be improved to accurately predict the PV refrigeration system performance, it can be used for sizing system components properly to meet the load requirements under the meteorological conditions of the operating site location.

11. ACKNOWLEDGEMENTS

The authors wish to express their sincere gratitude to the Government of Denmark for providing the financial support for this research work. The authors gratefully acknowledge the support given by the AIT Energy Park and WHO for allowing them to use the Environmental Test Chamber and the PV vaccine refrigeration system throughout this research. Thanks are also extended to Prof. R.H.B. Exell and Dr. Surapong Chirarattanong for their valuable comments during the course of this research.

REFERENCES

1. Zaffran, M. (1993), Solar Energy for Primary Health Care, *Solar Energy and Health - Working Papers*, WHO report submitted to the High-level Expert Meeting of World Solar Summit, Paris, France, 5-9 July 1993, pp. 237-248.
2. Lambarski, T.J. and Bradwell (1980), PV TAP: a Program for Performing Electrical and Thermal Analysis on Photovoltaic Elements, *Proceedings of 14th IEEE PV Specialists Conference*, San Diego, California, 7-10 January 1980, IEEE, New York.
3. Das, A.K. (1982), *Evaluation of Electrical and Thermal Parameters of Solar Cells and Modules*, AIT Special Study Report No. ET 1982-9, Energy Technology Division, Asian Institute of Technology, Bangkok, Thailand.
4. Jet Propulsion Laboratory (1976), *Thermal Performance Testing and Analysis of Photovoltaic Modules in Natural Sunlight*, California Institute of Technology, Pasadena, California, U.S.A.
5. Lasnier, F., T.G. Ang and K.S. Lwin (1988), *Technical Social and Economic Evaluation of Photovoltaic Systems for Rural Application: Solar Photovoltaic Handbook*, Energy Technology Division, Asian Institute of Technology, Bangkok, Thailand.
6. Mayer, A. and S. Biscaglia (1989), Modelling and Analysis of Lead Acid Battery Operation, *Proceedings of the 9th EC PV Solar Energy Conference*, Freiburg, F.R.G., 25-29 September 1989, Kluwer Academic Publishers, London.
7. Komp, R.J. (1981), *Practical Photovoltaic: Electricity from Solar Cells*, Aatec Publication, Ann Arbor, Michigon, U.S.A., pp. 42-52.
8. Specialty Concepts Inc.(1986), *Installation and Operation Manual for the SCI Charger Series Regulators*, Canoga Park, U.S.A.
9. Kilfoyle, D., B. Marion and G.G. Venture (1990), Lessons Learned from Testing Photovoltaic Vaccine Refrigerators, *Proceedings of 21st IEEE PV Specialists Conference*, May 1990, IEEE, New York, pp. 985-990.
10. *Danfoss Direct Current Compressors 12V and 24 V*, Danfoss Technical Specification sheet CN.16.G3.02. Danfoss A/S, Nordbong, Denmark.
11. Charters, W.W.S. and Aye Lu (1990), Performance Prediction of a Small-Scale Photovoltaic Refrigerator, *RERIC International Energy Journal*, Vol. 12, No. 2, pp. 65-74.
12. Bato-On, M.C. (1992), *Small-Scale Stand-Alone Photovoltaic Refrigeration System Simulation*, AIT Thesis No. ET 1992-12, Energy Technology Division, Asian Institute of Technology, Bangkok, Thailand.
13. Twidell, J.W. and A.D. Weir (1986), *Renewable Energy Resources*, Chapter 7, pp. 143-177, Spon., London.
14. Ang, T.G. (1984), *Analysis of a Compression Refrigeration Supplied by Photovoltaic Power*, AIT Thesis No. ET 1984-10, Energy Technology Division, Asian Institute of Technology, Bangkok, Thailand.
15. NASA – LEWIS Research Center (1977), *Revised Terrestrial Photovoltaic Measurement Procedures, TM73702*, Scientific and Technical Information Division, NASA, Washington, D.C., U.S.A.
16. WHO – Expanded Program on Immunization (1988), *Standard Equipment Specifications and Test Procedures*, EPI Technical series No.5.

APPENDIX - A

PV Array Model Parameters Determination

Procedures for determining various performance parameters of PV modules for use in the PV array model given in Section 1 are described in the following sections and the values of these parameters obtained for the PV modules used in this study are presented in the last section.

A.1 Series Resistance

Series resistance, R_s, can be estimated using the two light method. In this method, the I-V characteristics at two different solar radiation levels are considered. To illustrate the method, consider a positive increment δI, and add this to the short circuit currents I_{sc1} and I_{sc2}, i.e.

$$I_{sc1} + \delta I = I_{sc1} - I_0\left[\exp\left(\frac{V_1 - R_s\left(I_{sc1} + \delta I\right)q}{AkT_p}\right) - 1\right] \quad \text{(A1)}$$

and

$$I_{sc2} + \delta I = I_{sc2} - I_0\left[\exp\left(\frac{V_2 - R_s\left(I_{sc2} + \delta I\right)q}{AkT_p}\right) - 1\right] \quad \text{(A2)}$$

Equating the two expressions for δI, R_s can be calculated as

$$R_s = \left(\frac{V_1 - V_2}{I_{sc2} - I_{sc1}}\right) \quad \text{(A3)}$$

Bato-on [12] has emphasized the importance of selecting the values of I_{sc1} and I_{sc2} at two widely different radiation levels, in order to minimize the possible errors.

A.2 Shunt Resistance

Shunt resistance, R_{sh}, can be estimated considering the slope of I-V curve at the current generating region as given in the PV Handbook by Lasnier et al. [5].

$$R_{sh} = \left(\frac{V_2 - V_1}{I_{p1} - I_{p2}}\right)_{I_p \to I_{sc}} \quad \text{(A4)}$$

The I-V curve chosen should be at the normal cell operating temperature in order to avoid undue deviations.

A.3 Diode Ideality Factor

Das [3] presented a method for the estimation of the diode ideality factor, A. In this method V_{oc} at two different solar radiation levels, but at the same temperature are used to solve for A. The following are the two expressions for open circuit voltage at two radiation levels:

$$V_{oc1} = \frac{AkT_{p1}}{q} \ln\left[\frac{I_{sc1}}{I_{o1}} + 1\right] \quad \text{(A5)}$$

and

$$V_{oc2} = \frac{AkT_{p2}}{q} \ln\left[\frac{I_{sc2}}{I_{o2}} + 1\right] \quad \text{(A6)}$$

When $T_{p1} = T_{p2}$, $I_{o1} = I_{o2}$. Subtracting V_{oc1} of Eq.(A5) by V_{oc2} of Eq.(A6), the value of A can now be solved as

$$A = \left[\frac{q}{kT_p}\right]\left[\frac{V_{oc1} - V_{oc2}}{\ln(I_{sc1} / I_{sc2})}\right] \quad \text{(A7)}$$

A.4 Coefficients P_1, P_2, and P_3 Short Circuit Current

With the knowledge of three V-I curves at different temperatures and solar radiation intensities, the constant coefficients, P_1, P_2 and P_3, can be estimated by direct substitution. In this study 500 W/m^2 and 298 K were selected as the reference solar radiation and cell temperature, respectively.

A.5 Coefficient B for Reverse Saturation Current

Reverse Saturation Current, I_o can be estimated by using the numerical iteration method proposed by Bato-on [12]. In this method, with other parameters known, trial values of I_o are tested for an I-V curve at a particular module temperature. The value of I_o which results in a minimum standard error for I_p is selected. Initial trail value of I_o can be estimated from the fact that $I_o \sim 1\text{x}10^{-8}$ A/m^2 at 298 K for commercial PV cells. Subsequent values of I_o at different temperatures are also obtained by the same method. These I_o values are then fit to the exponential formula given in Eq.(3) and the value of B can be determined. The method was used and verified by Twidell [13] and Ang [14]).

A.6 View Factors and Emissivities

The typical values of the view factors and emissivities used in this study were adopted from the results of extensive research done by NASA [15] and the Jet Propulsion Laboratory [4] for calculation of radiation heat loss (Q_{rad}) and convective heat loss (Q_{conv}); those are $F_{pg} = F_{ps} = 1$, $E_p = 0.88$, $E_g = 0.90$ and $E_s = 1.00$.

A.7 Wind Speed

As the wind speed data is not intended to be provided as an input for the simulation program, instantaneous wind speed in Eq.(7) was replaced by the average wind velocity. Recorded average wind speed at the AIT Energy Park where the experimental set-up was located, was found to be 0.4 m/s.

A.8 Temperature Coefficient of Module Efficiency

The value of γ can be estimated from the manufacturer's data using

$$\gamma = \left[\frac{P_{T_r} - P_{T_p}}{P_{T_r}(T_p - T_r)} \right] \quad \text{(A8)}$$

where P_{Tr} = Module peak power at the reference temperature (W) and P_{Tp} = Module peak power at T_p (W). In this study, the reference temperature was taken as 298 K and the module efficiency η at the reference temperature was assumed as 14%. Although the estimated value of Q_{elect} using the above method is only a rough approximation, its effect on the accuracy of T_p is very small. This is because the electrical energy output is only a small fraction of the total incident solar energy.

A.9 Overall Absorption Coefficient

The value of α_{abs} can be estimated by numerical iteration, as was done in solving for I_o in Section A.5. First, the module temperatures at different solar radiation levels but under steady conditions are experimentally found. Under the above conditions, the left hand side of Eq.(4) becomes zero. After knowing all other parameters for module temperature model, the value of α_{abs} which gives minimum standard error with the experimental results is selected.

A.10 Effective Heat Capacity of the Module

In order to evaluate mCp_{module}, it is required to carry out a transient test. In the test, a covered PV module at low temperature was suddenly exposed to the steady solar radiation and the module temperature was recorded every two minutes. Then by fitting the experimental data into Eq.(4), mCp_{module} can be found.

A.11 Results of Determination of Model Parameters of PV Modules

The PV array of the system under investigation consisted of 4 Arco Solar M75 PV modules and 2 Photowatt BPX47402 PV modules, all connected in parallel. Procedures outlined in Sections A.1 through A.10 were used to compute the parameters for Arco Solar M75 and Photowatt BPX47402 PV modules. The results obtained are summarized in Table A1.

Table A1. Parameters obtained for two PV modules used in the study.

Parameters	Arco Solar M75	Photowatt BPX47402
Diode ideality factor (A)	37.11	38.59
Series resistance (R_s)	0.955 Ω	1.45 Ω
Shunt resistance (R_{sh})	260 Ω	200 Ω
Coefficients for short circuit current (I_{sc})		
P_1	$3.278*10^{-3}$ m²/W	$2.59*10^{-3}$ m²/V
P_2	$-0.5*10^{-5}$ m²/W	$-0.73*10^{-5}$ m²/W
P_3	$1.0*10^{-3}$ /K	$1.09*10^{-3}$ /K
Coefficient B for reverse saturation current (I_o)	4750 A/K³	7100 A/K³
Total surface area of the module (S_p)	0.3773 m²	0.4577 m²
Total area occupied by the cells in the module (S_c)	0.3401 m²	0.3598 m²
Temperature coefficient of module efficiency (γ)	0.0039 /K	0.0041 /K
Overall absorption coefficient of the module (α_{abs})	0.75	0.79
Convective heat transfer coefficient (H)	4.5294 W/m².K	4.5294 W/m².K

APPENDIX - B

Battery Model Parameters Determination

B.1 Parameters of Battery Capacity Model

Empirical constants b_1, b_2 and b_3 in Eq.(15) can be estimated using data given in the manufacturer's spec sheet, which gives the battery capacity under several charging rates. The constants b_1, b_2 and b_3 can be found by least square fitting of these data into Eq.(15).

B.2 Parameters of the Models for E_{oc} and R_b – Discharging Mode

A discharge test should be performed to find the parameters VF_d, VS_d of Eq.(12) and d_1 through d_4 of Eq.(20). In this study, the battery was discharged at a constant rate. Battery current (I_b), open circuit voltage (E_{oc}) and terminal voltage (V_b) were measured at the end of every 15 minute interval. The test was continued until E_{oc} reached 10.8V, which was the end of discharge voltage specified by the manufacturer. State of Charge of the battery at the end of each 15 minute interval was computed by summing up the charge released by the battery, assuming zero SOC at E_{oc} = 10.8V.

VF_d and VS_d can be estimated by fitting the SOC and corresponding E_{oc} values into Eq.(12). Rearranging Eq.(11), the battery internal resistance during the discharge can be expressed as

$$R_d = \frac{V_b - E_{oc}}{I_b} \qquad \text{(B1)}$$

Using the experimental data, R_b values at the end of each discharging interval were computed. By fitting these data (R_d and SOC) into Eq.(20), values of the constants (d_1 through d_4) can be estimated.

B.3 Parameters of the Models for E_{oc} and R_b – Charging Mode

A similar test as described in Section B.2 is required to be performed for the charging mode, in order to find the values of VF_c, VS_c, c_1, c_2, c_3 and c_4. In the test, starting from fully discharged condition (at the end of discharge test), the battery was charged at the same rate as in the discharging test. The test was stopped when the electrolyte gained its original specific gravity, which it possessed before starting the discharge test. The SOC after each charging interval was computed by summing up the charge flow, as explained in Section B.2. VF_c and VS_c can be estimated by least square fitting of open circuit voltage data into Eq.(12).

Values of R_c were evaluated using the relationship,

$$R_c = \frac{V_b - E_{oc}}{I_b} \qquad \text{(B2)}$$

By least square fitting of these R_c values and their corresponding values SOC into Eq.(19), the parameters (c_1 through c_4) for the charging resistance can be estimated.

B.4 Results of Determination of Model Parameters of Battery

In the study, two BP solar model PVSTOR 6P207 were used. Each has a nominal voltage of 6V and nominal capacity of 207 ampere-hours. They were connected in series to have 12 V to match with the refrigerator operating voltage. The values of various model parameters evaluated using the above mentioned procedures are presented in Table B1.

Table B1. Parameters obtained for the battery used in this study.

Battery Capacity		
$b_1 = 114.9$	$b_2 = 0.1575$	$b_3 = 0.5600$
Open Circuit Voltage		
$VF_c = 13.44$ V		$VS_c = 0.699$ V
$VF_d = 12.86$ V		$VS_d = 0.712$ V
Internal Resistance		
$c_1 = 0.0219$ ohms		$d_1 = 0.0039$ ohms
$c_2 = 0.0565$ ohms		$d_2 = 0.0335$ ohms
$c_3 = 85.638$ ohms^{-1}		$d_3 = 2.769$ ohms^{-1}
$c_4 = 72.670$ ohms^{-1}		$d_4 = -102.99$ ohms^{-1}

APPENDIX - C

Refrigerator Model Parameters Determination

C.1 Test Procedure

A series of tests has to be performed on the refrigerator, under a controlled environment in order to estimate 6 heat transfer coefficients and 4 heat capacities in the heat transfer network. The tests carried out in this study were designed to comply with the WHO test procedure for PV refrigerators [17] as far as possible. The intention of this was to make use of the test results obtained using WHO test procedures in estimation of the refrigerator model parameters. But due to the specific nature of the requirements some modifications and additions had to be made to the WHO standard test procedure.

The adopted test procedure consisted of two basic tests, which were repeated at three different ambient temperatures; 15°C, 32°C, and 43°C. Relative humidity (RH) was maintained between 55% and 65% at all temperatures.

In the first test (Test-1), the refrigerator loaded with ice-packs and vaccine load was allowed to be stabilized at the interested ambient temperature. Then both the compressors were connected to the 12 V dc supply and T_a, T_{wr}, T_{wf}, T_{vl}, T_{ip}, P_r and P_f were recorded at every five-minute interval. Temperatures were measured using type-T thermocouples attached to the respective places in the cabinet. The test was continued at least for 24 hours after reaching the steady running condition.

In the second test (Test-2), a 2.54 cm thick polystyrene foam insulation sheet was inserted into the space between the vaccine load and the refrigerator door, so that any heat flow into the vaccine load, except through the wall, was passed through this insulation sheet. Two additional thermocouple sensors were attached to either side of the insulation sheet to measure the temperature difference across it. After stabilizing at the ambient temperature, only the compressor for the vaccine storage side was supplied with 12 V dc power. The freezer compressor was kept at 'stop' throughout the experiment. Again the test was continued for 24 hours after reaching the steady running condition.

C.2 Determination of Heat Transfer Coefficients

In calculation of the heat transfer coefficients, the steady running period of the two tests were considered. First, 24 hour average values of all the temperatures and the powers under stable running condition were found from the test results. In the following discussion all the temperature and power values are referred to these stable running state average values.

Over the stable running period, the integrations of dT_{wr}/dt, dT_{wf}/dt, dT_{vl}/dt, dT_{ip}/dt in the Eqs.(25), (26), (27), (28) and (29), respectively over the stable running period were zero. In Test-2, heat gained to the vaccine compartment wall from the ambience via vaccine load was equal to the heat passing through the insulation sheet, P_{in}. Knowing the UA value of the insulation sheet (0.085 W/K), P_{in} could be calculated using the measured temperature difference across it.

It was noted that the difference between T_{vl} and T_{wr} i.e. $(T_{vl} - T_{wr})$ was approximately the same for both tests at a particular ambient temperature. It suggested that heat gain to the wall through the vaccine load is approximately equal to P_{in} even in Test-1. Therefore, an approximate value for

$UA_{a\text{-}wr}$ could be calculated from Eq.(25), using the results of Test-1, neglecting heat transfer between the refrigerator and freezer walls:

$$UA^*_{a\text{-}wr} = (P_r - P_{in}) / (T_a - T_{wr}) \quad \text{(C1)}$$

where $UA^*_{a\text{-}wr}$ = Approximate estimation of $UA_{a\text{-}wr}$.

A similar value could be found for $UA_{a\text{-}wf}$ from Eq.(26), when neglecting the heat transfer between two walls:

$$UA^*_{a\text{-}wf} = P_f / (T_a - T_{wf}) \quad \text{(C2)}$$

where $UA^*_{a\text{-}wf}$ = Approximate estimation of $UA_{a\text{-}wf}$.

After calculating the above approximate values, heat transfer between the refrigerator and the freezer walls was considered. The actual value of $UA_{a\text{-}wr}$ should be greater than $UA^*_{a\text{-}wr}$ found from Eq.(C1). Taking δP as the additional heat gain due to this difference, for Test-1, Equation (25) was rewritten as

$$0 = UA_{wf\text{-}wr}(T_{wf} - T_{wr}) + [UA^*_{a\text{-}wr}(T_a - T_{wr}) + \delta P] + P_{in} - P_r \quad \text{(C3)}$$

A similar equation could be written considering the results of Test-2, assuming that δP was approximately the same in both tests. These two simultaneous equations were solved for δP and $UA_{wf\text{-}wr}$.

When considering Eqs.(C1) and (C3), it could be observed that

$$\delta P = UA_{wf\text{-}wr}(T_{wr} - T_{wf}) \quad \text{(C4)}$$

which meant that the heat transfer between two walls was equal to δP. Therefore, the approximate values of the two heat transfer coefficients, $UA_{a\text{-}wr}$ and $UA_{a\text{-}wf}$, were corrected considering the results of Test-1:

$$UA_{a\text{-}wr} = (P_r + \delta P - P_{in}) / (T_a - T_{wr}) \quad \text{(C5)}$$

$$UA_{a\text{-}wf} = (P_f - \delta P) / (T_a - T_{wr}) \quad \text{(C6)}$$

From Test-2, $UA_{a\text{-}vl}$ and $UA_{vl\text{-}wr}$ were estimated as

$$UA_{a\text{-}vl} = P_{in} / (T_a - T_{vl}) \quad \text{(C7)}$$

$$UA_{vl\text{-}wr} = P_{in} / (T_{vl} - T_{wr}) \quad \text{(C8)}$$

It was observed that, the value of $UA_{a\text{-}wf}$ was dependent on the situation, whether the freezer was operating or not. The value of $UA_{a\text{-}wf}$ calculated under the conditions of Test-1 (both refrigerator and freezer were working), did not satisfy the conditions of Test-2 (only refrigerator was working). Since a situation where only the refrigerator is working, can be encountered during the actual operation (when the ice-packs cannot be frozen due to insufficient battery state of charge, the freezer has to be switched off), another set of $UA_{a\text{-}wf}$ were calculated considering the second test:

$$UA'_{a\text{-}wf} = UA_{wf\text{-}wr}(T_{wf} - T_{wr}) / (T_a - T_{wf}) \quad \text{(C9)}$$

where $UA'_{a\text{-}wf}$ = Value of $UA_{a\text{-}wf}$ when freezer is not in operation (W/K).

The reason for having two different values for UA_{a-wf} comes from the difference in the heat flow pattern in the cabinet wall at these two situations. Although two lumped heat capacities, refrigerator wall and freezer wall, were defined to represent the cabinet wall, there is no physical boundary between them. Therefore, their actual values depend on the heat flow pattern. When the freezer is operating, the temperature around the freezer inner wall is lower than that around the refrigerator and more heat flows towards the freezer. But when it is not operating, the temperature around the refrigerator inner wall is lower than that around the freezer, changing the heat flow pattern in the opposite way. This causes it to have a smaller UA_{a-wf} when the freezer is not operating than its normal value when both refrigerator and freezer are running.

The other possible situation where only the freezer is operating, is not considered in this study. This situation arises rarely in real operation because the refrigerator should be running as long as vaccine is stored in it.

C.3 Determination of Heat Capacities

With the knowledge of the above mentioned heat transfer coefficients, heat capacities were estimated considering the initial cool down period of Test-1. the summation of energy flows in Eq.(25) obtained at an interval time δt, throughout the period during which the temperature of the refrigerator wall drops from T_{wr1} to T_{wr2} gave

$$mC_{pwr} = \left[\sum_{T_{wr}=T_{wr1}}^{T_{wr2}} UA_{vl-wr} (T_{vl} - T_{wr}) \delta t + \sum_{T_{wr}=T_{wr1}}^{T_{wr2}} UA_{a-wr} (T_a - T_{wr}) \delta t + \sum_{T_{wr}=T_{wr1}}^{T_{wr2}} UA_{wf-wr} (T_{wf} - T_{wr}) \delta t - \sum_{T_{wr}=T_{wr1}}^{T_{wr2}} P_r \delta t \right] \frac{1}{(T_{wr2} - T_{wr1})} \quad \text{(C10)}$$

mC_{pwf} and mC_{pvl} were also estimated in a similar manner using Eqs.(26) and (27). Heat capacity of the ice-packs was taken as $m_{ip}{}^{*}C_{pw}$. The remaining parameter UA_{ip-wf} was also calculated considering the transient part. Considering the initial cool down period, during which the ice-pack temperature dropped from T_{ip1} to T_{ip2}, summation of energy flows in Eq.(29) gave

$$UA_{ip-wf} = \frac{m_{ip} C_{pw} (T_{ip2} - T_{ip1})}{\sum_{T_{ip}=T_{ip1}}^{T_{ip2}} (T_{ip} - T_{wf}) \delta t} \quad \text{(C11)}$$

C.4 Results of Determination of Model Parameters of Refrigerator

It was found from the tests under diffrent controlled ambienttemperatures that the evaluated parameters, UA_{a-wr}, UA_{a-wf}, UA_{a-vl}, mC_{pwr} and mC_{pwf} varied with the ambient temperature. Variation of UA_{vl-wr}, UA_{ip-wf}, UA_{wf-wr} and mC_{pvl} with the temperature was negligible. The results are summarized in Table C1.

Table C1. Refrigerator model parameters obtained from the tests at different ambient temperatures.

Parameter	15°C	32°C	43°C
UA_{a-wr} (W/K)	0.41	0.47	0.68
UA_{a-wf} (W/K)	0.24	0.37	1.27
UA_{a-vl} (W/K)	0.036	0.037	0.040
UA_{vl-wr} (W/K)	0.90	0.90	0.90
UA_{ip-wf} (W/K)	1.30	1.30	1.30
UA_{wf-wr} (W/K)	0.10	0.10	0.10
UA'_{a-wf} (W/K)	0.27	0.26	0.23
mC_{pwr} (J/K)	12,800	13,300	19,500
mC_{pwf} (J/K)	3,850	4,850	6,000
mC_{pvl} (J/K)	9,000	9,000	9,000